https://doi.org/10.5194/egusphere-2026-1088
Preprint. Discussion started: 8 April 2026

Contrail formation for aircraft with hydrogen combustion - Part 3: A neural-network-based parameterization of ice crystal number

Josef Zink[1], Cornelius Weiß-Rehm[1], Simon Unterstrasser[1], and Ulrike Burkhardt[1]
[1]Deutsches Zentrum für Luft- und Raumfahrt, Institut für Physik der Atmosphäre, Oberpfaffenhofen, Germany
Correspondence: Josef Zink (josef.zink@dlr.de)

Abstract. Contrail cirrus clouds are a major contributor to the climate impact of aviation. Large-scale models, such as general circulation models (GCMs) with an integrated contrail module, are used to estimate the radiative forcing of these clouds. However, small-scale processes cannot be explicitly resolved in these models and must therefore be parameterized. In this study, we develop a novel parameterization for the number of contrail ice crystals formed on ambient aerosols entrained into the exhaust plume behind aircraft burning hydrogen. The continuous entrainment of ambient aerosols, combined with higher supersaturation in hydrogen exhaust plumes, results in longer-lasting ice crystal formation than in conventional kerosene combustion, where ice crystals predominantly form on emitted soot. We construct the parameterization from a comprehensive database of time-resolved contrail formation simulations conducted with the Lagrangian Cloud Module in a box model approach. Shallow neural networks are used to reproduce the simulation outcome, complemented by analytical scaling relations to extend the applicability of the parameterization. The parameterization incorporates dependencies on ambient conditions, ambient aerosol properties and aircraft-related parameters. We compare the new parameterization with an existing one originally developed for conventional kerosene combustion that treats ice crystal formation as a single nucleation pulse. The comparison reveals that the assumption of a nucleation pulse is not reasonable for hydrogen combustion scenarios. We find it essential to base the parameterization on time-resolved simulations, as this realistically captures ice crystal formation on continuously entrained ambient aerosols.

1 Introduction

1.1 Motivation

Aviation currently contributes about $3.5\,\%$ to the anthropogenic radiative impact on climate (Lee et al., 2021). More than half of this impact arises from non-CO_2 effects, with contrail cirrus clouds being the dominant contributor to the radiative forcing (Lee et al., 2021; Kärcher, 2018; Paoli and Shariff, 2016). To quantify their radiative forcing, general circulation models (GCMs) have been extended with contrail modules (Burkhardt and Kärcher, 2009; Gettelman and Chen, 2013; Schumann et al., 2015; Bock and Burkhardt, 2016). Since processes occurring on scales below the grid resolution cannot be resolved, cloud processes need to be parameterized within GCMs. This applies to cloud microphysics in general and, in particular, to the early stages of contrail formation and the interaction of young contrails with the lift-induced wake vortices. The key quantity during the early contrail stage is the number of ice crystals, which strongly influences the evolution and the radiative effect of persistent contrail cirrus (Unterstrasser and Gierens, 2010; Lewellen, 2014; Bier et al., 2017; Burkhardt et al., 2018; Lottermoser and Unterstrasser, 2025).

For conventional kerosene combustion, parameterizations have been developed for both the formation of ice crystals (Kärcher et al., 2015) and their loss due to wake vortex interactions (Unterstrasser, 2016). These parameterizations have been implemented into the GCM with contrail parameterization, ECHAM-CCMod (Bier and Burkhardt, 2019, 2022). Since, thermodynamics and microphysics are substantially different for hydrogen combustion scenarios (Bier et al., 2024; Zink et al., 2025a), these parameterizations must be adapted or newly developed. Recently, Lottermoser and Unterstrasser (2025) extended the ice crystal loss parameterization to account for scenarios with hydrogen-powered aircraft. The present study introduces a new parameterization for the number of ice crystals formed in the exhaust plume of aircraft burning hydrogen.

1.2 Scope and outline of the study

Here we literally repeat the according subsection "Scope and outline of the study" of Part 1 (see Sect. 1.2 in Zink et al. (2025a)): "Our overarching goal is to develop a parameterization for the final number of ice crystals formed for aircraft with hydrogen combustion, suitable for implementation in GCMs and other large-scale contrail models. Specifically, we seek a functional relationship of the form

$$N_{\mathrm{ice,f}} = N_{\mathrm{ice,f}}(\mathbf{a}_{\mathrm{atmosphere}}, \mathbf{a}_{\mathrm{aerosol}}, \mathbf{a}_{\mathrm{aircraft}}) \;, \tag{1}$$

where $\mathbf{a}_{\mathrm{atmosphere}}$ denotes a set of variables characterizing the background atmosphere (e.g., ambient temperature), $\mathbf{a}_{\mathrm{aerosol}}$ represents properties of ambient aerosols (number concentration, size distribution and solubility) and $\mathbf{a}_{\mathrm{aircraft}}$ includes aircraft-related parameters (e.g., engine size).

Our objective is to identify a functional relationship that balances simplicity with physical fidelity. In other words, we aim to capture the impact of the key processes that govern ice crystal formation in a form that is simple enough to be easily applied in other models (level of complexity, computing time, ease of implementation). In Parts 1 and 2 of a trilogy of papers, we systematically explore a broad parameter space and address aspects that have not been explored before to gain a deep insight into the physical processes influencing the ice crystal formation. This allows us to select the set of variables that constitute the inputs to the parameterization of $N_{\mathrm{ice,f}}$.

While a previous $N_{\mathrm{ice,f}}$ parameterization of contrail formation (Kärcher et al., 2015) used a first-principles-based concept, the current work across Parts 1 to 3 employs a hybrid approach. It combines a data-driven advanced regression method to fit a multidimensional database of contrail formation simulations with analytical scaling relations. To keep the number of dimensions in the simulation database as small as possible, we identify conditions under which the sensitivity to specific variables is negligible, and also employ analytical scaling relations derived from sensitivity simulations.

In Part 1, we focus on the roles of atmospheric variables $\mathbf{a}_{\mathrm{atmosphere}}$ and aerosol properties $\mathbf{a}_{\mathrm{aerosol}}$. Aircraft-related parameters $\mathbf{a}_{\mathrm{aircraft}}$ are addressed in Part 2. The final parameterization, synthesizing insights from Parts 1 and 2, will be presented in Part 3."

https://doi.org/10.5194/egusphere-2026-1088
Preprint. Discussion started: 8 April 2026

The parameterization developed in the present study is based on neural networks, which serve as fitting functions for the outcomes of the contrail formation simulations. Our target quantity is the final number of ice crystals formed, i.e., the number when ice crystal formation is completed in our simulations. In previous studies, we distinguished the final number $N_{\mathrm{ice,f}}$ from the time-dependent number $N_{\mathrm{ice}}(t)$. Since we only consider the final number here, we omit the subscript "f" throughout the paper, except in this introduction and in the conclusion (Sect. 5).

Sections 2.1 to 3.1 provide technical details on the configuration, training, and evaluation of the neural networks. Readers mainly interested in the final results with physical discussion may continue directly with Sect. 3.2, where we compare upper-tropospheric profiles of simulated and parameterized ice crystal numbers. Sect. 3.3 summarizes scaling relations derived in Parts 1 and 2, which are used to generalize the parameterization (with a practical step-by-step cookbook of how to employ the parameterization presented in Appendix A). In Sect. 4.1, we compare our approach with an existing parameterization that was originally developed for kerosene combustion but is applied here to hydrogen combustion. Finally, we discuss strengths and limitations of the developed parameterization in Sect. 4.2 before concluding in Sect. 5.

2 Data and Methods

2.1 Training and verification data

Our database consists of contrail formation simulations performed with the Lagrangian Cloud Module (LCM) in a box model approach (Bier et al., 2022, 2024). In this approach, dilution, which governs plume expansion and cooling, is prescribed externally. The microphysics is then calculated in a time-resolved manner without feedback on the plume dynamics. In the particle-based LCM, aerosol particles and hydrometeors (liquid droplets and ice crystals) are represented by simulation particles (SIPs), with each SIP corresponding to a certain number of real physical particles.

We use simulation results covering all possible combinations of variable values listed in Table 1. This results in a dataset with $\prod_{i=1}^{6} n_i > 20,000$ entries, where n_i denotes the number of values sampled for variable i. A physical description of this dataset is given in Zink et al. (2025a). This gridded dataset is used to train a regression neural network (Sect. 2.2.1). Using the gridded data ensures that the model is trained within well-defined variable bounds set by the minimum and maximum values of each input variable.

To evaluate the model performance on an independent data set that was not used for training, we generate an additional $\prod_{i=1}^{6}(n_i - 1) > 5,000$ simulations at randomly sampled points located between the grid points (Fig. 1). This dataset serves to assess how well the trained model performs in-between the gridded *training data*. In our study, we refer to this entire off-grid dataset as the *verification dataset*. Following standard machine learning practice, we divide it equally into two subsets: a *validation set*, used for hyperparameter tuning during training (see Sect. 2.2.1 for details), and a *testing set*, used only for evaluating the best performing model. While the term verification is common in physical modeling, validation and testing are the conventional terms in machine learning to describe these specific roles.

Table 1. LCM box model simulation results for all possible combinations of listed variable values are used as training dataset. For the verification dataset, simulations were performed for random data points between the gridded data points (Fig. 1). Parameters that were not varied are also listed (indicated with asterisks).

variable	**values**
ambient temperature T_a / K	210, 215, 220, 225, 230, 232.5, 234.5
ambient pressure p_a / hPa	150, 230, 320, 400
ambient relative humidity over ice $RH_\mathrm{ice,\,a}$ / %	100, 115, 125, 140
aerosol number concentration n_aer / $\mathrm{cm^{-3}}$	1, 10, 100, 1000, 10000
aerosol geometric mean radius $\overline{r}_\mathrm{d,\,aer}$ / nm	1, 2, 5, 10, 20, 40, 100, 200, 500
aerosol hygroscopicity κ_aer / −	0.01, 0.05, 0.25, 1.25
fixed parameters	
aerosol geometric width $\sigma^*_\mathrm{aer} = 1.6$	water vapor emission index $EI^*_\mathrm{v} = 8.94\,\mathrm{kg\,kg^{-1}}$
specific combustion heat $Q^* = 120\,\mathrm{MJ\,kg^{-1}}$	overall propulsion efficiency $\eta^* = 0.4$
aircraft speed $U^*_\infty = 250\,\mathrm{m\,s^{-1}}$	excess jet velocity $U^*_\mathrm{jet,E} = 230\,\mathrm{m\,s^{-1}}$
core exit radius $r^*_\mathrm{E} = 0.5\,\mathrm{m}$	core exit temperature $T^*_\mathrm{E} = 580\,\mathrm{K}$

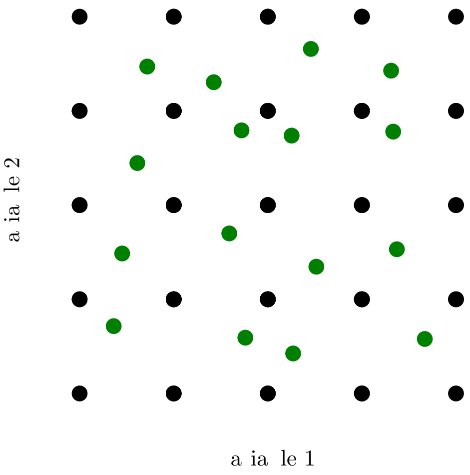

Figure 1. Schematic illustration of training (black) and verification (green) datasets.

2.2 Design of neural networks for parameterizing the ice crystal number

90 Neural networks provide a flexible framework for capturing nonlinear relationships, without requiring an explicit analytical form. This makes them particularly well suited for approximating intricate dependencies that classical fitting methods might

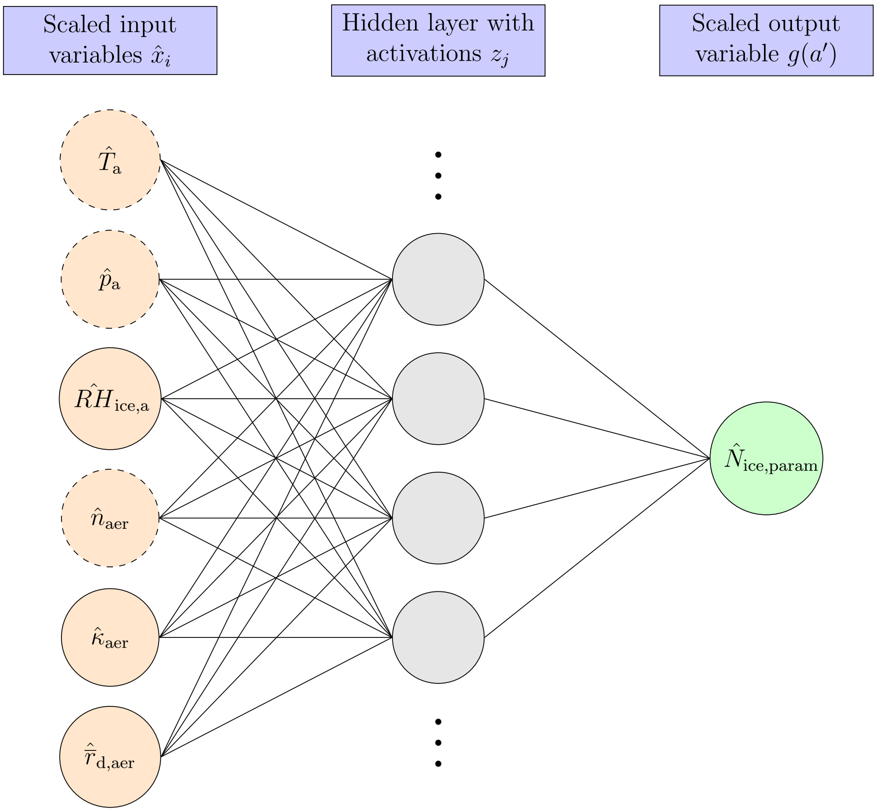

Figure 2. Schematic depiction of the employed Multilayer Perceptron. For both the FullNet and ClassificationNet, all depicted input variables are used. The ReducedNet uses only the input variables marked by dashed circles.

struggle to represent. For this reason, we chose a shallow, fully connected feedforward artificial neural network, known as a Multilayer Perceptron (MLP), to approximate the number of ice crystals as a function of the predictors listed in Table 1. To limit the total number of trainable parameters (fit parameters/coefficients), we restrict the architecture to a single hidden layer (Fig. 2). 95

The corresponding calculations are given by (Bishop, 2019)

$$a_j = \sum_{i=1}^{n_\mathrm{inputs}} \hat{x}_i w_{ij} + \beta_j \tag{2a}$$

$$z_j = f(a_j) \tag{2b}$$

$$a' = \sum_{j=1}^{n_\mathrm{nodes}} z_j w'_j + \beta' \tag{2c}$$

$$\hat{N}_\mathrm{ice,param} = g(a') \quad . \tag{2d}$$

https://doi.org/10.5194/egusphere-2026-1088
Preprint. Discussion started: 8 April 2026

For each hidden-layer node j, the (scaled) inputs $\hat{x}_i$ are linearly combined (Eq. (2a)) using the weights w_{ij} and biases β_j. In classical regression approaches, w_{ij} and β_j would be named fit parameters/coefficients. The resulting pre-activation values a_j are then passed through a nonlinear activation function f (Eq. (2b)), yielding the hidden-layer activations z_j. These activations are again linearly combined (Eq. (2c)) and passed through the (possibly nonlinear) output activation function g (Eq. (2d)) to produce the network output $\hat{N}_{\mathrm{ice,param}}$. This sequence of operations applies to both a regression network (Sect. 2.2.1) and a classification network (Sect. 2.2.2), with $\hat{N}_{\mathrm{ice,param}}$ having different interpretations in each case.

2.2.1 Regression neural network

In a regression neural network, $\hat{N}_{\mathrm{ice,param}}$ is a continuous variable representing the (scaled) number of ice crystals as a function of the scaled inputs $\hat{x}_i$. The inputs x_i are scaled to $\hat{x}_i$ to improve training efficiency and enhance the performance of the resulting model. As a first scaling step, all inputs describing aerosol properties (number concentration, geometric mean radius, hygroscopicity) are log-transformed

$$\tilde{x}_i = \log_{10}(x_i) \tag{3}$$

to account for the several orders of magnitude spanned by their prescribed values. The remaining inputs (ambient temperature, ambient pressure, ambient relative humidity) are left unchanged at this step ($\tilde{x}_i = x_i$). After this initial transformation, all resulting inputs $\tilde{x}_i$ are standardized according to

$$\hat{x}_i = \frac{\tilde{x}_i - \mu_{\tilde{x}_i}}{\sigma_{\tilde{x}_i}} \quad , \tag{4}$$

where $\mu_{\tilde{x}_i}$ and $\sigma_{\tilde{x}_i}$ are the mean and standard deviation of the input variable ranges. This standardization ensures that all inputs have comparable magnitudes and variability.

In addition to the scaling of the input variables, we also include a scaling of the output variable $\hat{N}_{\mathrm{ice}}$, which can vary over several orders of magnitude (Zink et al., 2025a). Since the mean squared error is used as the loss function during training (see Eq. (8)), cases with low ice crystal numbers would contribute very little to the overall (absolute) error if no output scaling were applied. Consequently, these low-number cases might be neglected during optimization of the weights and biases. To avoid this, we apply a 'hybrid' output transformation: Below a tuneable critical constant $N_{\mathrm{ice,crit}}$, a logarithmic scaling is used, while above it, a linear approximation applies. Using the logistic function (Fig. 3a)

$$\sigma(y) = \frac{1}{1 + e^{-\alpha(y - y_0)}} \quad , \tag{5}$$

these two regimes are smoothly connected by a sigmoidal transition (Fig. 3b), expressed as

$$\hat{N}_{\mathrm{ice}} = [1 - \sigma(y)]\log_{10}(y) + \sigma(y)[cy + d] \tag{6}$$

with $y = N_{\mathrm{ice}}/N_{\mathrm{ice,crit}}$. In our case, $y_0 = 1$ and α is a tuning parameter. The parameters $c = 1/\ln(10)$ and $d = -c$ in Eq. (6) ensure a smooth and differentiable transition between the logarithmic and linear regimes as $\alpha \to \infty$. This hybrid transformation accounts for low ice crystal numbers without loss of accuracy in the high-number range, where the linear approximation is valid.

https://doi.org/10.5194/egusphere-2026-1088
Preprint. Discussion started: 8 April 2026

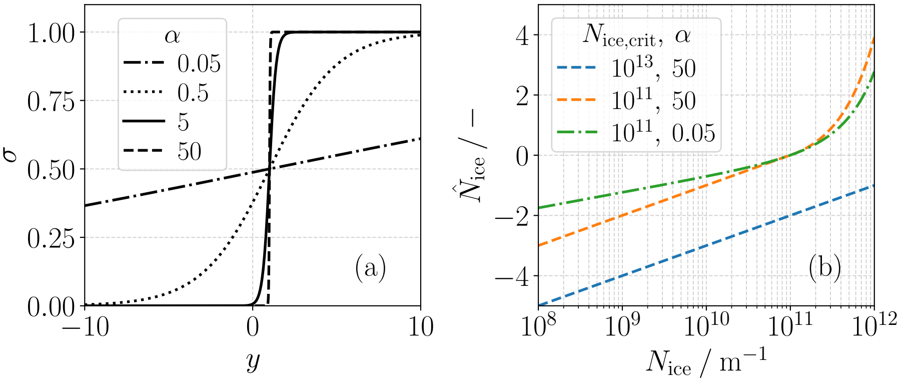

Figure 3. (a) Logistic function (Eq. (5)) for different α values and (b) hybrid coordinate transformation (Eq. (6)) for different $N_{\mathrm{ice,crit}}$ and α values.

In summary, the trained neural network predicts the scaled values $\hat{N}_{\mathrm{ice,param}}$ from the scaled inputs $\hat{x}_i$ (Fig. 2). The final ice crystal number $N_{\mathrm{ice,param}}$ is then obtained by applying the inverse transformation of Eq. (6).

In a regression problem, the output activation function g is typically the identity. If the activation function of the hidden layer f were also the identity, the entire neural network would effectively reduce to a classical multiple linear regression model. However, to capture the nonlinear relationship between the ice crystal number and the inputs, a nonlinear function f is needed. We experimented with several common nonlinear activation functions (Tanh, Logistic function, Softmax, ReLU, Leaky ReLU, ELU). We found that the choice of activation function has only a minor impact on the final model performance. Consequently, we select the rectified linear unit (ReLU) defined as

$$f(a_j) = \max(0, a_j) \tag{7}$$

due to its simplicity and low computational cost.

During the training process, the loss function

$$\mathcal{L}_{\boldsymbol{\gamma}}(\mathbf{w};\boldsymbol{\beta}) = \frac{1}{N}\sum_{k=1}^{N}\left(\hat{N}_{\mathrm{ice,param}}(\hat{\mathbf{x}}_k;\mathbf{w};\boldsymbol{\beta};\boldsymbol{\gamma}) - \hat{N}_{\mathrm{ice,sim},k}\right)^2 + \lambda\|\mathbf{w}\|^2 \tag{8}$$

is minimized by computing its gradients with respect to the weights and biases via the backpropagation algorithm, and updating the weights and biases using the gradient descent rule (Bishop, 2019). This update procedure is repeated over multiple iterations, called epochs. In Eq. (8), the first term represents the mean squared error between the scaled training data $\hat{N}_{\mathrm{ice,sim},k}$ and the neural network predictions $\hat{N}_{\mathrm{ice,param}}(\hat{\mathbf{x}}_k;\mathbf{w};\boldsymbol{\beta};\boldsymbol{\gamma})$. Here, $\hat{\mathbf{x}}_k$ is the vector of scaled input variables $\hat{x}_i$ for simulation k, $\mathbf{w}$ denotes the collection of all weights (matrix elements w_{ij} and vector elements w'_j), $\boldsymbol{\beta}$ represents the biases (vector elements β_j and scalar β') and $\boldsymbol{\gamma}$ stands for a set of hyperparameters. The second term acts as a regularization penalty, with $\|\mathbf{w}\|^2$ being the squared Euclidean norm of the weights (i.e., the sum of squares of all weights) and λ the regularization parameter. This term prevents excessively large weights and thus helps to prevent overfitting to the training data (Bishop, 2019). We trained the network for 300 epochs and selected the weights and biases from the epoch with the lowest validation loss as the final model parameters. We found that training beyond 300 epochs does not yield further improvements.

While Eq. (8) is used internally during the training process, we evaluate the final model performance after applying the inverse transformation of Eq. (6), i.e., on the unscaled data. For this evaluation, we use the absolute percentage error (APE), defined as

$$\mathrm{APE}_k = \frac{|N_{\mathrm{ice,param},k} - N_{\mathrm{ice,sim},k}|}{N_{\mathrm{ice,sim},k}} \cdot 100\% \tag{9}$$

where $N_{\mathrm{ice,sim},k}$ and $N_{\mathrm{ice,param},k}$ are the simulated and parameterized values for simulation k, respectively. We then summarize the errors across the dataset of interest by computing the median absolute percentage error

$$\mathrm{MdAPE} = \mathrm{Median}\left(\{\mathrm{APE}_k\}\right) \;. \tag{10}$$

We use Eq. (10) as the criterion for selecting the best-performing model. This final model consists of the trained weights and biases together with a set of optimized hyperparameters. Hyperparameters are model constraints that are specified a-priori and not updated during training. Consequently, different models can be trained and compared, each with a distinct set of hyperparameters. In our case, the hyperparameters of interest include the number of hidden layer nodes n_{nodes}, the regularization parameter λ, and the hybrid-coordinate parameters $N_{\mathrm{ice,crit}}$ and α. The model with the set of hyperparameters minimizing Eq. (10) on the validation set is chosen as the final model.

In the end, we provide two regression neural networks: The *FullNet* is trained on all cases with $N_{\mathrm{ice,sim}} > 0$ and uses the six predictors listed in Table 1. It is applicable across the full range of training data. The *ReducedNet* is trained only within the subspace defined by $T_{\mathrm{a}} \leq 225\,\mathrm{K}$ and $10\,\mathrm{nm} \leq \overline{r}_{\mathrm{d,\,aer}} \leq 100\,\mathrm{nm}$. In this regime, the number of ice crystals formed is largely independent of ambient relative humidity, aerosol size, and aerosol hygroscopicity (Zink et al., 2025a). Consequently, the ReducedNet uses only three predictors (marked by dashed circles in Fig. 2): ambient temperature, ambient pressure, and aerosol number concentration.

2.2.2 Classification neural network

In several simulations for ambient temperatures $T_{\mathrm{a}} > 230\,\mathrm{K}$, aerosols activate into liquid droplets but none of these droplets freeze into ice crystals ($N_{\mathrm{ice,sim}} = 0$). In cases where ice crystals form in this temperature range, their numbers are typically in the range from $\sim 10^{8}\,\mathrm{m}^{-1}$ to $\sim 10^{11}\,\mathrm{m}^{-1}$, resulting in an abrupt transition from zero to large ice crystal numbers depending nonlinearly on the inputs. This discontinuous behavior is challenging to capture using a single regression model, as it would require a complex network with a large number of fit parameters to resolve the sharp jump accurately. To manage this, the regression model FullNet is trained only on samples with strictly positive ice crystal numbers ($N_{\mathrm{ice,sim}} > 0$). For these cases, the dependence of ice crystal number on the inputs is smoother and can be approximated well by the regression network without excessive model complexity. To explicitly separate the binary nature of ice formation from the continuous variation in ice crystal number, we introduce a classification network (hereinafter named as *ClassificationNet*). This network is trained to separate between cases with $N_{\mathrm{ice,sim}} = 0$ and $N_{\mathrm{ice,sim}} > 0$.

The simulated ice crystal number is converted into a binary variable via

$$\tilde{N}_{\text{ice,sim}} = \begin{cases} 1 & \text{if } N_{\text{ice,sim}} > 0 \\ 0 & \text{otherwise.} \end{cases} \tag{11}$$

The output activation function g of the ClassificationNet is the logistic function (Eq. (5)) and the resulting output $\hat{N}_{\text{ice,param}}$, ranging from zero to one, is interpreted as the probability that ice crystals form for a given set of inputs $\hat{\mathbf{x}}$. During the training, the regularized binary-cross entropy loss

$$\mathcal{L}_{\boldsymbol{\gamma}}(\mathbf{w};\boldsymbol{\beta}) = -\frac{1}{N}\sum_{k=1}^{N}\left[\tilde{N}_{\text{ice,sim},k}\log\left(\hat{N}_{\text{ice,param}}(\hat{\mathbf{x}}_k;\mathbf{w};\boldsymbol{\beta};\boldsymbol{\gamma})\right) + (1-\tilde{N}_{\text{ice,sim},k})\log\left(1-\hat{N}_{\text{ice,param}}(\hat{\mathbf{x}}_k;\mathbf{w};\boldsymbol{\beta};\boldsymbol{\gamma})\right)\right] + \lambda\|\mathbf{w}\|^2 \tag{12}$$

is minimized by updating the network weights $\mathbf{w}$ and biases $\boldsymbol{\beta}$. The first term inside the summation penalizes misclassifications when ice crystals have formed in the simulation (false negatives), while the second term penalizes misclassifications when no ice crystals are present (false positives). As for the regression network, the regularization term $\lambda\|\mathbf{w}\|^2$ prevents overfitting by discouraging excessively large weight values.

In the regression task, the continuous variation of ice crystal numbers (for values greater than zero) allows effective training on a gridded dataset by fitting a smooth curve. In the binary classification problem, however, the target variable takes only two values, so no meaningful interpolation between grid points is possible. Therefore, we combine all gridded and off-gridded data described in Sect. 2.1 for $T_\text{a} \geq 230\,\text{K}$ (> 10,000 simulations) and randomly split the combined dataset into training, validation, and test sets with proportions of $70\,\%$, $15\,\%$, and $15\,\%$, respectively. Furthermore, the combined dataset contains more simulations with $\tilde{N}_{\text{ice,sim}} = 1$ ($\sim 83\,\%$). To balance the classes during training, we randomly subsample the training set with $\tilde{N}_{\text{ice,sim}} = 1$ to match the number of simulations with $\tilde{N}_{\text{ice,sim}} = 0$, which helps prevent the model from being biased toward the majority class.

The probabilistic network output $\hat{N}_{\text{ice,param}}$ is finally converted into a binary variable

$$\tilde{N}_{\text{ice,param}} = \begin{cases} 1 & \text{if } \hat{N}_{\text{ice,param}} \geq 0.5 \\ 0 & \text{otherwise.} \end{cases} \tag{13}$$

With this binary variable, we evaluate the false negative rate

$$\text{FNR} = \frac{\sum(\tilde{N}_{\text{ice,param}} = 0\,|\,\tilde{N}_{\text{ice,sim}} = 1)}{\sum(\tilde{N}_{\text{ice,sim}} = 1)} \cdot 100\% \tag{14}$$

and the false positive rate

$$\text{FPR} = \frac{\sum(\tilde{N}_{\text{ice,param}} = 1\,|\,\tilde{N}_{\text{ice,sim}} = 0)}{\sum(\tilde{N}_{\text{ice,sim}} = 0)} \cdot 100\% \tag{15}$$

as an evaluation of the model performance.

https://doi.org/10.5194/egusphere-2026-1088
Preprint. Discussion started: 8 April 2026

3 Results

3.1 Hyperparameter tuning

In this section, we briefly summarize the optimization process for the hyperparameters n_{nodes}, λ, $N_{\mathrm{ice,crit}}$, and α. Starting from an initial set of values, we vary one hyperparameter at a time while keeping the others fixed, selecting the value that yields the best performance. We then proceed to optimize the next hyperparameter using the best values found so far. After cycling through all hyperparameters, we repeat the process starting again from the first. We found that only a few such cycles are necessary before further iterations no longer produce a significant reduction in error.

Fig. 4 illustrates the hyperparameter tuning for the FullNet. The MdAPE initially decreases sharply with increasing number of nodes n_{nodes} for both the training and validation sets (Fig. 4a). The validation set exhibits a local minimum at $n_{\mathrm{nodes}} = 43$, beyond which no significant improvement is observed. Hence, this value is chosen to avoid unnecessarily increasing the total number of fit parameters (Eqs. (2a)–(2d)).

For the regularization parameter λ, the validation set shows a minimum in MdAPE at $\lambda = 10^{-3}$, with increasing error toward both higher and lower values (Fig. 4b). Interestingly, the training error also increases as λ decreases, which is somewhat unexpected since the training error is typically lowest for $\lambda = 0$. This behavior can be explained by the fact that the loss function applied on the scaled data during training (Eq. (8)) differs from the error metric we use to evaluate the final model performance on the unscaled data (Eq. (10)).

Regarding $N_{\mathrm{ice,crit}}$, the MdAPE is high at low values (Fig. 4c) due to large errors in low ice crystal number cases when the linear regime extends over a wide range in the hybrid coordinate transformation (Eq. (6)). The error decreases until $N_{\mathrm{ice,crit}} \sim 10^{11}\,\mathrm{m}^{-1}$, with a slight dependence on the choice of α. Although the pair $N_{\mathrm{ice,crit}} = 3\cdot 10^{11}\,\mathrm{m}^{-1}$ and $\alpha = 0.5$ yields a marginally lower MdAPE than $N_{\mathrm{ice,crit}} = 10^{11}\,\mathrm{m}^{-1}$ and $\alpha = 5$, we select the latter pair to maintain the linear regime over a broader range of ice crystal numbers.

The advantage of the hybrid-coordinate transformation becomes particularly clear when considering only cases with $N_{\mathrm{ice,sim}} > 10^{11}\,\mathrm{m}^{-1}$. The MdAPE of these cases is reduced from $10.9\,\%$ to $7.1\,\%$ for the validation set when switching from a fully logarithmic scaling ($N_{\mathrm{ice,crit}} \to \infty$) to the hybrid-coordinate transformation with $N_{\mathrm{ice,crit}} = 10^{11}\,\mathrm{m}^{-1}$ and $\alpha = 5$.

We performed the same hyperparameter tuning for the ReducedNet (considering also the MdAPE) and for the ClassificationNet (considering FNR and FPR). The final selected values are summarized in Table 2, together with the corresponding errors for the training, validation, and testing datasets. The close agreement between training and validation errors indicates no significant overfitting to the training data. The similarity between validation and testing errors demonstrates strong generalization of the developed models.

This is further supported by the cumulative distribution functions (CDFs) of the APE for the regression networks, which show that the distributions for the training set and the verification set (validation and testing sets together) are very similar (Fig. 5). For the subspace defined by $T_{\mathrm{a}} \leq 225\,\mathrm{K}$ and $10\,\mathrm{nm} \leq \overline{r}_{\mathrm{d,\,aer}} \leq 100\,\mathrm{nm}$ the CDFs for the ReducedNet and the FullNet are nearly identical up to the ∼80th percentile of the APE. This is notable given the ReducedNet has a strongly reduced total number of weights and biases (Table 2). Beyond the 80th percentile of the error distribution, the FullNet exhibits slightly

https://doi.org/10.5194/egusphere-2026-1088
Preprint. Discussion started: 8 April 2026

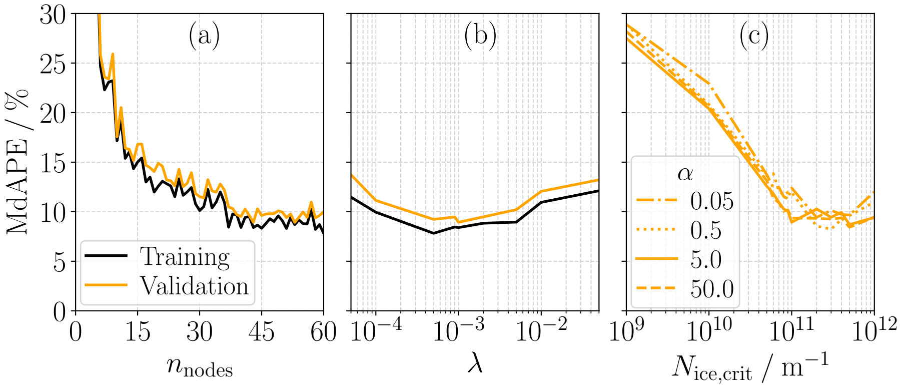

Figure 4. Median absolute percentage error (MdAPE) for the FullNet for the training (black) and validation (orange) dataset as a function of (a) node number n_nodes (b) regularization parameter λ and (c) hybrid-coordinate parameters $N_\mathrm{ice,crit}$ and α. For the sake of clarity, only results for the validation data are depicted in (c). The hyperparameters are fixed to $n_\mathrm{nodes} = 43$, $\lambda = 10^{-3}$, $N_\mathrm{ice,crit} = 10^{11}\,\mathrm{m}^{-1}$ and $\alpha = 5$ except in the panel where they are varied.

Table 2. Best found hyperparameters, total number of fit coefficients (weights and biases) n_coeff, and corresponding training, validation and testing error for the different neural network types.

Network type	n_nodes	λ	$N_\mathrm{ice,crit}$ / m^{-1}	α	n_coeff	error (training/validation/testing)
FullNet	43	10^{-3}	10^{11}	5	345	$\mathrm{MdAPE} = 8.0/8.7/8.5\,\%$
ReducedNet	11	$9 \cdot 10^{-3}$	10^{11}	5	56	$\mathrm{MdAPE} = 5.5/5.0/5.2\,\%$
ClassificationNet	9	10^{-4}	-	-	73	$\mathrm{FNR} = 1.9/1.8/1.9\,\%$ $\mathrm{FPR} = 1.5/1.4/1.3\,\%$

smaller errors than the ReducedNet within this subspace. This difference arises because near the defined boundaries of the subspace, the ice crystal number becomes increasingly sensitive to the input variables omitted in the ReducedNet. Omitting these sensitivities leads to slightly larger errors. Hence, applying the ReducedNet instead of the FullNet for the given subspace is a trade-off between the potential gain in computational speed and the accuracy of the parameterized values.

3.2 Upper-tropospheric profiles of simulated and parameterized ice crystal number

Table 3. Combination of ambient temperature and pressure values according to the International Standard Atmosphere (e.g., Etling, 2008).

altitude / km	8.2	8.6	9.0	9.4	9.8	10.2	10.6	11.0	12.2	13.2
T_a / K	234.85	232.25	229.65	227.05	224.45	221.85	219.25	216.65	216.65	216.65
p_a / hPa	345.81	326.16	307.42	289.56	272.55	256.36	240.96	226.32	187.30	159.97

https://doi.org/10.5194/egusphere-2026-1088
Preprint. Discussion started: 8 April 2026

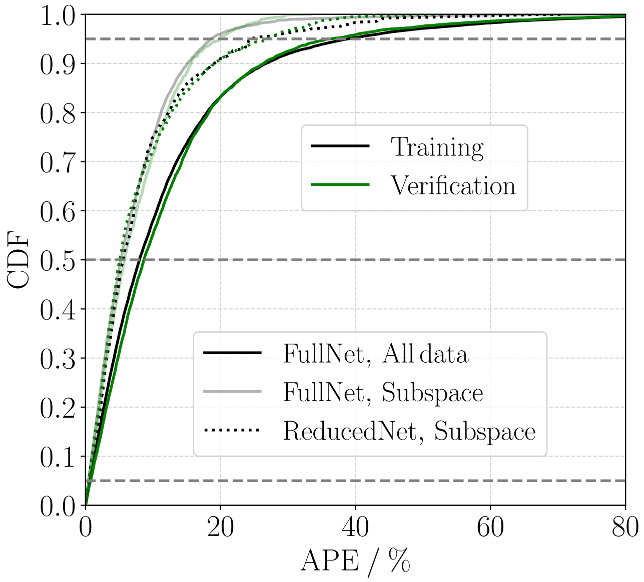

Figure 5. (a) Cumulative distribution function (CDF) of absolute percentage error (APE) for training (black color) and verification (testing and validation set together; green color) dataset. Shown are the CDFs for the FullNet evaluated with all data (solid opaque lines), for the FullNet evaluated within the subspace defined by $T_\mathrm{a} \leq 225\,\mathrm{K}$ and $10\,\mathrm{nm} \leq \overline{r}_\mathrm{d,\,aer} \leq 100\,\mathrm{nm}$ (transparent solid lines), and for the ReducedNet evaluated within this subspace (dotted opaque lines). Dashed horizontal lines indicate the 5th percentile, the median and the 95th percentile.

After the technical description of the neural networks in Sect. 2.2 and Sect. 3.1, we now visualize the results by comparing simulated and parameterized vertical profiles of the ice crystal number N_ice (Fig. 6). Ambient temperature and pressure are prescribed according to the International Standard Atmosphere (Table 3).

The neural network successfully reproduces the sensitivities to the various variables systematically investigated in Zink et al. (2025a). It captures the nearly linear increase of N_ice with aerosol number concentration n_aer at low n_aer, as well as the saturation effect at high n_aer (different colors in Fig. 6). It also reproduces the pronounced decrease in N_ice at low altitudes caused by high ambient temperatures. In the isothermal layer above $11\,\mathrm{km}$, the network reasonably reflects the occasional slight decrease of N_ice with increasing altitude, attributable to reduced pressure. Furthermore, it accounts for the decrease in N_ice for small aerosol sizes (second row in Fig. 6) due to the Kelvin effect, as well as the freezing point depression for well-soluble particles with a large dry radius (Fig. 6e).

The successful fit to the simulation data is achieved both for the FullNet across the entire parameter space considered and for the ReducedNet, applied to the subspace $T_\mathrm{a} \leq 225\,\mathrm{K}$ and $10\,\mathrm{nm} \leq \overline{r}_\mathrm{d,aer} \leq 100\,\mathrm{nm}$ (first row in Fig. 6).

3.3 Generalizing the parameterization

The neural networks were derived for a scenario with a single aerosol population and a reference engine/aircraft as characterized by the parameters listed in Table 1. The parameterization can be generalized by incorporating several scaling relations. The

https://doi.org/10.5194/egusphere-2026-1088
Preprint. Discussion started: 8 April 2026

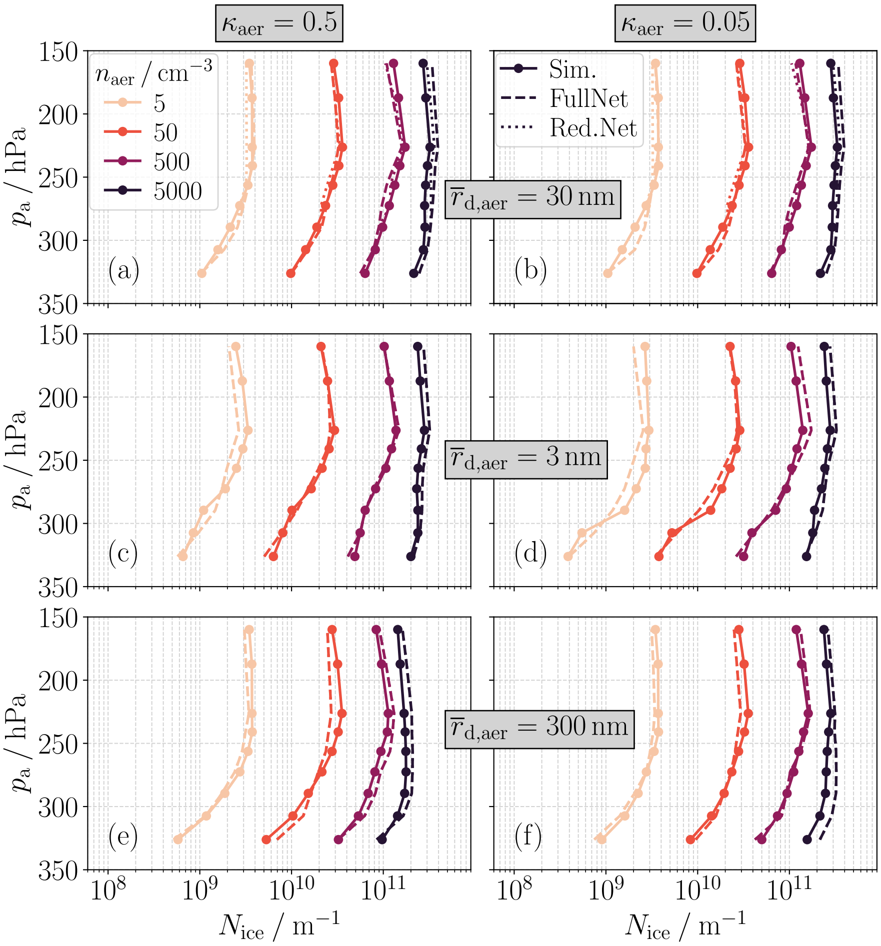

Figure 6. Simulated and parameterized ice crystal number N_{ice} as a function of different aerosol number concentrations n_{aer} (different colors), different aerosol geometric mean radii $\overline{r}_{\mathrm{d,aer}}$ (different rows) and different hygroscopicities κ_{aer} (different columns). Ambient pressure p_{a} and temperature T_{a} values are set according to the International Standard Atmosphere (Table 3), and ambient relative humidity is fixed to $RH_{\mathrm{ice,a}} = 120\,\%$. The outcome of the FullNet is shown in all panels, while the ReducedNet is additionally applied in the first row for cases with $T_{\mathrm{a}} \leq 225\,\mathrm{K}$. Results are shown for $N_{\mathrm{ice}} > 0$.

physical basis of all proposed scaling relations has been discussed in detail in Part 1 (Zink et al., 2025a) and Part 2 (Zink and Unterstrasser, 2025) and is briefly summarized here.

In Part 1, we showed that we can mimic the effect of multiple coexisting aerosol populations by the weighted mean approach

$$N_{\mathrm{ice,tot}} \approx \sum_i \frac{n_{\mathrm{aer},i}}{n_{\mathrm{aer,tot}}} N_{\mathrm{ice},i}(n_{\mathrm{aer,tot}}) \ , \tag{16}$$

where $N_{\mathrm{ice},i}(n_{\mathrm{aer,tot}})$ is the ice crystal number obtained from a simulation that includes only population i with its hygroscopicity $\kappa_{\mathrm{aer},i}$ and geometric mean dry radius $\overline{r}_{\mathrm{d,aer},i}$ but with assumed total aerosol number concentration $n_{\mathrm{aer,tot}} = \sum_i n_{\mathrm{aer},i}$. In practice, the neural networks are separately called for each population using $\kappa_{\mathrm{aer},i}$ and $\overline{r}_{\mathrm{d,aer},i}$ together with $n_{\mathrm{aer,tot}}$. The outputs are then combined through the weighted mean approach (Eq. (16)) to represent the effect of multiple co-existing aerosol populations.

The neural networks provide the ice crystal number for an engine with a reference overall propulsion efficiency of $\eta^* = 0.4$ (Table 1). In Part 2, we demonstrated that the effect of a different efficiency η on the ice crystal number can be mimicked by keeping η^* but adjusting the pressure according to

$$p_{\mathrm{a,adj}} = p_{\mathrm{a}} \frac{1-\eta^*}{1-\eta} \ . \tag{17}$$

We showed that this scaling works reasonably well for tested η-values in the range from 0.325 to 0.475. Consequently, to represent efficiencies different from η^*, the neural networks are called with the adjusted pressure $p_{\mathrm{a,adj}}$.

Moreover, the neural networks return the ice crystal number for a reference engine size and jet speed (Table 1). In Part 2, we introduced scaling factors that account for differences in jet speed s_{shear} and engine size s_{E} relative to the reference values with associated change in dilution speed s_{dil}. These scaling factors are defined as

$$s_{\mathrm{shear}} = U^*_{\mathrm{jet,E}} / U_{\mathrm{jet,E}} \tag{18a}$$

$$s_{\mathrm{E}} = r_{\mathrm{E}} / r^*_{\mathrm{E}} \tag{18b}$$

$$s_{\mathrm{dil}} = s_{\mathrm{shear}} \cdot s_{\mathrm{E}} \tag{18c}$$

$$\hat{s}_{\mathrm{E}} = s_{\mathrm{E}} \cdot \sqrt{U_{\mathrm{tot,E}} U^*_{\infty} / (U^*_{\mathrm{tot,E}} U_{\infty})} \tag{18d}$$

with $U_{\mathrm{tot,E}} = U_{\mathrm{jet,E}} + U_{\infty}$. The scaling factor $\hat{s}_{\mathrm{E}}$ accounts for the fact that the number of entrained ambient aerosols scales with the effective core exit area $\hat{A}_{\mathrm{E}} = A_{\mathrm{E}} U_{\mathrm{tot,E}} / U_{\infty}$ (see Eq. (12) in Zink and Unterstrasser (2025)). If only this effective core area were scaled without any change in dilution speed, then the number of ice crystals would scale simply with $\hat{s}^2_{\mathrm{E}}$.

In Part 2 we introduced the scaling

$$\frac{N_{\mathrm{ice}}}{\hat{s}^2_{\mathrm{E}} \cdot s^a_{\mathrm{dil}}} \sim f(s^{3/2}_{\mathrm{dil}} \cdot n_{\mathrm{aer}}) \tag{19}$$

with

$$a = \begin{cases} -\frac{3}{2} & \text{for } T_{\mathrm{a}} \leq 230\,\mathrm{K} \\ \frac{1}{6}\,(T_{\mathrm{a}}/\mathrm{K} - 239) & \text{for } 230\,\mathrm{K} < T_{\mathrm{a}} \leq 235\,\mathrm{K} \ . \end{cases} \tag{20}$$

The function f depends on ambient conditions and aerosol properties but not explicitly on the engine size/dilution speed. This means that the curves for different $\hat{s}_{\mathrm{E}}$ and s_{dil} values collapse when the scaling is applied. Practically, the neural networks are evaluated with the input $s_{\mathrm{dil}}^{3/2} \cdot n_{\mathrm{aer}}$ and the resulting ice crystal number is multiplied by $\hat{s}_{\mathrm{E}}^2 \cdot s_{\mathrm{dil}}^a$ to represent non-reference engine size and jet speed.

In practical applications, information about engine size and jet speed may not always be available. As a first-order approximation, the fuel consumption per meter of flight path m_{C} can then be used to estimate s_{E}. Here, m_{C} refers to the fuel consumption of a single engine, i.e.,

$$m_{\mathrm{C}} = \frac{m_{\mathrm{C,tot}}}{n_{\mathrm{engines}}} \ , \tag{21}$$

where $m_{\mathrm{C,tot}}$ is the total fuel consumption of the aircraft and n_{engines} the number of engines. Since $m_{\mathrm{C}} \propto s_{\mathrm{E}}^2/\eta$, it follows the approximation

$$\hat{s}_{\mathrm{E}} \approx s_{\mathrm{dil}} \approx s_{\mathrm{E}} \approx \sqrt{m_{\mathrm{C}}\eta/(m_{\mathrm{C}}^{*}\eta^{*})} \ . \tag{22}$$

Clearly, this approximation implicitly assumes similar excess jet speeds and ratios of total jet speed to aircraft speed.

The weighted mean approach (Eq. (16)) and the scaling associated with jet speed and engine size (Eq. (19)) were tested independently in Parts 1 and 2. The former was applied only to the reference engine (Table 1), while the latter was tested for a single aerosol population. Here, we propose combining the two scalings. The validity of using them together is exemplarily demonstrated in Fig. 7. The figure shows results from LCM box model simulations including two aerosol populations with the size s_{E} of the reference engine (Table 1) scaled both up and down. These simulations are compared to parameterized values obtained through the step-by-step cookbook described in Appendix A. The results are presented from three perspectives: First, scaling according to Eq. (19) shows that the simulated curves for different engine sizes almost collapse onto a single curve (i.e., the scaling associated with the engine size also holds for coexisting aerosol populations). This is well approximated by the parameterized curves, which become identical under this scaling (Fig. 7a). Second, scaling only by the geometric scale $\hat{s}_{\mathrm{E}}$ highlights the influence of the dilution speed s_{dil} (Fig. 7b). Third, the unscaled ice crystal numbers represent the final quantities of interest (Fig. 7c). The simulated curves are reasonably approximated by the parameterized values demonstrating that the weighted mean approach remains valid for engine sizes differing from the reference. Clearly, this is also true if the jet speed had been varied.

The validity of the neural networks is guaranteed only within the variable ranges listed in Table 1. When applying the scalings, care must be taken to avoid extrapolation (for example, the aerosol number concentration supplied as input to the neural networks should not exceed $10000\,\mathrm{cm}^{-3}$).

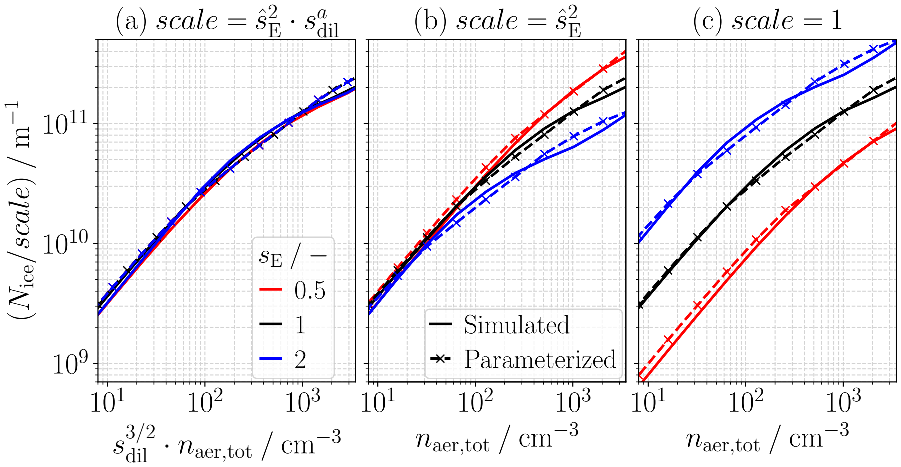

Figure 7. Number of ice crystals per meter of flight path N_ice as a function of (scaled) total aerosol number concentration $n_\mathrm{aer,tot}$. Results from box model simulations including two aerosol populations ($\overline{r}_\mathrm{d,\,aer,1} = 30\,\mathrm{nm}$, $\overline{r}_\mathrm{d,\,aer,2} = 3\,\mathrm{nm}$, $\kappa_\mathrm{aer,1} = 0.5$, $\kappa_\mathrm{aer,2} = 0.05$, $\sigma_{\mathrm{aer},i} = 1.6$, $n_\mathrm{aer,1} : n_\mathrm{aer,2} = 1:1$) are compared to the parameterized values following the cookbook described in Appendix A. Different engine sizes s_E are considered (with $\hat{s}_\mathrm{E} = s_\mathrm{dil} = s_\mathrm{E}$). Ambient temperature, ambient pressure and ambient relative humidity are set to $T_\mathrm{a} = 225\,\mathrm{K}$, $p_\mathrm{a} = 260\,\mathrm{hPa}$ and $RH_\mathrm{ice,a} = 115\,\%$, respectively. (a) Scaling after Eq. (19), (b) Scaling of N_ice by the geometric scale $\hat{s}_\mathrm{E}^2$, (c) Unscaled data.

4 Discussion

4.1 Comparison with existing parameterization

4.1.1 The K15 model

Kärcher et al. (2015) developed a microphysical model describing contrail ice crystal formation during the jet phase, hereinafter referred to as the K15 model. The K15 parameterization was designed for conventional kerosene or alternative fuels with soot emissions within the soot-rich regime (defined as a regime where ice crystal formation on soot particles dominates) and estimates the number of ice crystals forming on soot and ambient aerosol particles. This parameterization was integrated into the GCM ECHAM-CCMod for studying the radiative forcing of contrails in soot-rich scenarios (Bier and Burkhardt, 2019, 2022). By setting the soot emission index to zero and replacing the combustion-specific parameters with hydrogen values (specific combustion heat $Q = 120\,\mathrm{MJ\,kg^{-1}}$ and water vapor emission index $EI_\mathrm{v} = 8.94\,\mathrm{kg\,kg^{-1}}$), the model framework was adapted by Pettersson et al. (2025) to study hydrogen combustion scenarios. Using this adaptation, they employed the K15 model for contrail formation on ambient aerosol and lubrication oil particles. They integrated the outcomes of the K15 model into the Contrail Cirrus Prediction model (CoCiP) (Schumann, 2012) to assess the energy forcing of contrail cirrus from hydrogen combustion. In the following, this hydrogen-adapted model is termed K15-H2, while K15 is used when referring to the model's general framework.

https://doi.org/10.5194/egusphere-2026-1088
Preprint. Discussion started: 8 April 2026

Unlike our data-driven approach (of fitting box model simulation data), K15 uses an approach based on first principles. The underlying physical laws (as implemented in the box model, e.g.) are reformulated and simplified such that the reduced equations can be solved analytically. In the subsequent paragraph, we briefly summarize the key idea of the K15 model; for a more comprehensive description, the reader is referred to the original publication.

Starting point is the differential equation for the plume supersaturation $s = S - 1$, where S is the saturation ratio over water (relative humidity over water given as ratio and not in percentage). This differential equation is expressed as

$$\frac{\mathrm{d}s}{\mathrm{d}t} = \mathcal{P} - \mathcal{L} \ . \tag{23}$$

Here, $\mathcal{P}$ denotes the net production of supersaturation, consisting of a dilution term that tends to decrease the supersaturation and a cooling term that tends to increase the supersaturation (Eq. (6) in Kärcher et al. (2015)). $\mathcal{L}$ denotes the microphysical condensation sink (Eq. (45) in Kärcher et al. (2015)).

The key idea of the K15 model is to determine the point in time at which the net production of supersaturation equals the condensation sink, i.e., when $\frac{\mathrm{d}s}{\mathrm{d}t} = 0$. The model first checks how many droplets would be required to satisfy $\mathcal{L} = \mathcal{P}$ at a given time t. As a second criterion, it checks how many plume particles could already activate into droplets according to κ-Köhler theory (Petters and Kreidenweis, 2007). The activation-relaxation point in time $t = t_{\mathrm{peak,K15}}$ is chosen, such that both criteria yield the same number concentration of activated particles $n_{\mathrm{act,peak,K15}}$. Here, we introduce the notion of a peak value of supersaturation, even though the K15 model itself is not time-resolved, in order to maintain a consistent naming convention with the terminology used to describe the results of the box model simulations in Sect. 4.1.2.

For $t < t_{\mathrm{peak,K15}}$, the K15 model assumes negligible water vapor depletion so that the supersaturation evolves as it would without microphysical sink terms. Moreover, it assumes that the number of activated aerosols is sufficient to quench supersaturation and no further droplet formation occurs beyond $t = t_{\mathrm{peak,K15}}$. In soot-rich scenarios, this assumption of instantaneous supersaturation relaxation is justified because the largest soot particles are already activated at $t = t_{\mathrm{peak,K15}}$ and rapidly reduce the supersaturation. As a result, the number of particles that would activate after $t = t_{\mathrm{peak,K15}}$ becomes negligible. However, this assumption of instantaneous supersaturation relaxation becomes questionable when aerosol emissions are reduced drastically.

Finally, the K15 parameterization assumes that all aerosols that activate at $t_{\mathrm{peak,K15}}$ subsequently freeze into ice crystals. This approximation is reasonable at the low temperatures at which kerosene contrails form, but becomes problematic at the higher temperatures at which hydrogen contrails can form as not all activated droplets may freeze.

As we report ice crystal numbers per meter of flight path in the present study, the number concentration $n_{\mathrm{act,peak,K15}}$ is converted into the integrated number of activated particles per meter of flight path, $N_{\mathrm{act,peak,K15}}$, by multiplying it with the plume cross-sectional area. The final number of ice crystals formed is then obtained by setting $N_{\mathrm{ice,K15}} = N_{\mathrm{act,peak,K15}}$.

4.1.2 Contrasting the two approaches

As the K15 parameterization was recently applied for hydrogen combustion (Pettersson et al., 2025), we compare this K15-H2 parameterization with our H2 parameterization of contrail ice crystals formed on entrained ambient aerosols. Across the

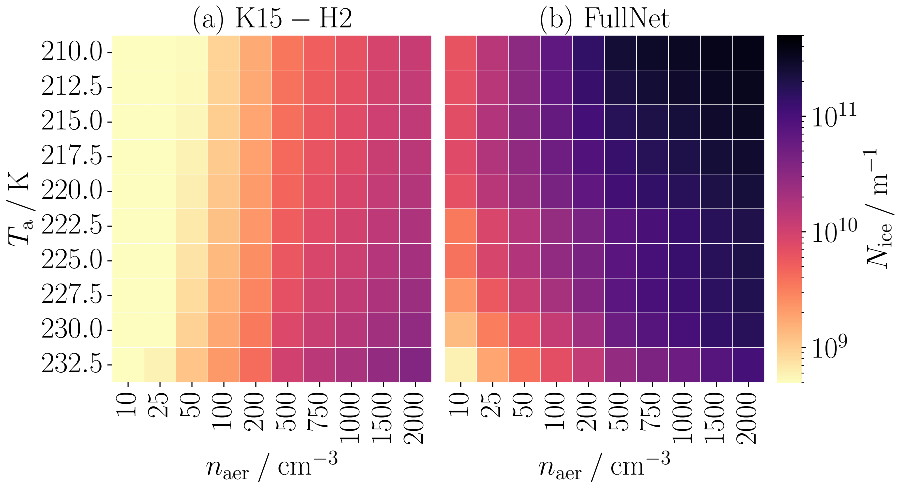

Figure 8. Number of ice crystals per meter of flight path N_{ice} for (a) the K15-H2 parameterization with $B = 0.9$ in Eq. (24) and (b) the outcome of the FullNet. Values are presented for selected combinations of ambient aerosol number concentration n_{aer} and temperature T_{a}.

two approaches, we consistently prescribe the parameters for aerosol geometric mean radius, geometric width, hygroscopicity, ambient pressure, and ambient relative humidity over ice. Their values are fixed at $\overline{r}_{\mathrm{d,aer}} = 20\,\mathrm{nm}$, $\sigma_{\mathrm{aer}} = 1.6$, $\kappa_{\mathrm{aer}} = 0.5$, $p_{\mathrm{a}} = 230\,\mathrm{hPa}$, and $RH_{\mathrm{ice,a}} = 115\,\%$, respectively. Engine-related parameters are set according to the reference values listed in Table 1 for which the neural networks are valid without any scaling needed.

Fig. 8 compares the ice crystal number obtained from the K15-H2 parameterization and from the FullNet, with both approaches using the same consistent parameter set. The ice crystal number differs substantially between the two parameterizations. While the magnitudes are comparable at high ambient temperatures, the K15-H2 parameterization gives ice crystal numbers up to two orders of magnitude lower at low ambient temperatures. Moreover, the dependence on ambient temperature is reversed between the two approaches: in the K15-H2 model, the ice crystal number increases with increasing temperature, whereas in our approach, the number decreases with increasing temperature.

The trends observed in the outcome of the FullNet are confirmed by underlying LCM box model simulations. To better understand and explain the differences between K15-H2 and our parameterization, we analyze the time-resolved droplet formation and freezing processes in our box model. For consistency, we prescribe the same analytical dilution formula in the box model setup as in K15-H2. This analytical formula for the dilution factor $\mathcal{D}$ reads

$$\mathcal{D}(t > \tau_{\mathrm{m}}) = \left(\frac{\tau_{\mathrm{m}}}{t}\right)^{B} \tag{24}$$

and $\mathcal{D} = 1$ for $t \leq \tau_{\mathrm{m}}$ with $\tau_{\mathrm{m}} \approx 0.01\,\mathrm{s}$. The exponent B determines the dilution speed, which can be adjusted both in K15 and in the box model. In K15, the default value $B = 0.9$ was proposed in Kärcher (1999). In Part 2 (Zink and Unterstrasser, 2025), it was shown that $B = 1.15$ yields closer agreement with the FLUDILES dilution data (Vancassel et al., 2014), which were used to construct the simulation database for the training of the neural networks. Furthermore, Fig. 8b in Part 2 demonstrates that ice crystal numbers obtained with $B = 1.15$ differ only marginally from those obtained with the FLUDILES data. We therefore prescribe each of the two values ($B = 0.9$ and $B = 1.15$) in K15-H2 and in our box model. This allows the effects of the underlying dilution data to be disentangled from those of the model physics.

Fig. 9a and 9b show selected examples of the evolution of plume relative humidity over water $RH_{\mathrm{wat}}(t)$ with the peak values $RH_{\mathrm{wat,peak}}$ highlighted. For the box model, two types of $RH_{\mathrm{wat}}(t)$ evolutions are depicted: a version with microphysics switched off (transparent lines) and the standard version with microphysical water vapor depletion (opaque lines). It is apparent that both types and the K15-H2 have a basically identical $RH_{\mathrm{wat}}(t)$ evolution up to the point in time $t = t_{\mathrm{peak,K15}}$. Hence, the box model results support the assumption of zero water vapor depletion in K15-H2 until $t = t_{\mathrm{peak,K15}}$. However, $RH_{\mathrm{wat,peak,K15}}$ (marked by a blue cross) is much lower and occurs earlier than the maximum relative humidity value within the box model, $RH_{\mathrm{wat,peak,box}}$ (marked by a magenta cross). At $t = t_{\mathrm{peak,box}}$, microphysical water vapor depletion is already pronounced, with the amount of depleted water vapor depending on the aerosol number concentration (difference between transparent and opaque magenta lines in Fig. 9a and b, respectively).

As the K15-H2 parameterization treats $t = t_{\mathrm{peak,K15}}$ as the point where further droplet activation ceases, $RH_{\mathrm{wat,K15}}$ is assumed to drop abruptly to $100\,\%$. In contrast to K15-H2, the box model results show that the supersaturation is not quenched at $t = t_{\mathrm{peak,box}}$ and supersaturation persist over an extended period.

Fig. 9c–d depicts the evolution of already activated aerosols $N_{\mathrm{act}}(t)$ (the sum of droplets and ice crystals in the box model). Since $t_{\mathrm{peak,K15}} < t_{\mathrm{peak,box}}$, it follows that $N_{\mathrm{act,peak,K15}} < N_{\mathrm{act,peak,box}}$. At $t = t_{\mathrm{peak,K15}}$, the number $N_{\mathrm{act,peak,K15}}$ equals $N_{\mathrm{act,box}}(t = t_{\mathrm{peak,K15}})$. Thus, both approaches yield a comparable number of activated aerosols up to this point in time. Within the box model, however, the activation of continuously entrained ambient aerosols extends over a longer period, such that the final number of ice crystals formed is not only considerably higher than $N_{\mathrm{act,peak,K15}}$ but also higher than $N_{\mathrm{act,peak,box}}$ (marked by a magenta cross).

After the illustrative example for the ambient temperature $T_{\mathrm{a}} = 220\,\mathrm{K}$, we now evaluate results across a range of T_{a} (Fig. 10). Fig. 10a–b shows the peak values of plume relative humidity $RH_{\mathrm{wat,peak}}$. These values decrease with increasing ambient temperature and higher aerosol number concentration. At low T_{a}, the K15-H2 parameterization yields substantially lower peak values than the box model and the dependence on dilution speed is reversed: in K15-H2, slower dilution ($B = 0.9$) yields higher peak values, while in the box model faster dilution ($B = 1.15$) does. This difference arises from the assumption of zero water vapor depletion for $t < t_{\mathrm{peak,K15}}$ in the K15-H2 model. Contrastingly, early activation in the box model already reduces water vapor until $t = t_{\mathrm{peak,box}}$ with slower dilution resulting in lower peak values.

For all investigated scenarios, it holds $t_{\mathrm{peak,K15}} < t_{\mathrm{peak,box}}$ (Fig. 10c-d). In the box model, the point in time $t_{\mathrm{supersat,end}}$ where $RH_{\mathrm{wat,box}}$ falls below $100\,\%$ is long after $t_{\mathrm{peak,box}}$. Moreover, t_{peak} gets larger with T_{a} (in both modeling approaches), while $t_{\mathrm{supersat,end}}$ generally decreases with T_{a}. At high T_{a} and slow dilution ($B = 0.9$), $t_{\mathrm{supersat,end}}$ increases with T_{a}. This can be attributed to the influence of the freezing timescale at these high temperatures (Zink and Unterstrasser, 2025).

Figures 10e–f show the mean radius of activated aerosols at $t = t_{\mathrm{peak,K15}}$. Already activated aerosols are much larger in K15-H2 than simulated by the box model at these points in time. This explains why supersaturation relaxation in the K15-H2 occurs before the relative humidity peaks in the box model: larger droplets provide enough surface area to remove supersaturation more quickly. Consequently, it holds $N_{\mathrm{act,peak,K15}} < N_{\mathrm{act,peak,box}}$ for all investigated scenarios (Fig.10g–h). However, in

https://doi.org/10.5194/egusphere-2026-1088
Preprint. Discussion started: 8 April 2026

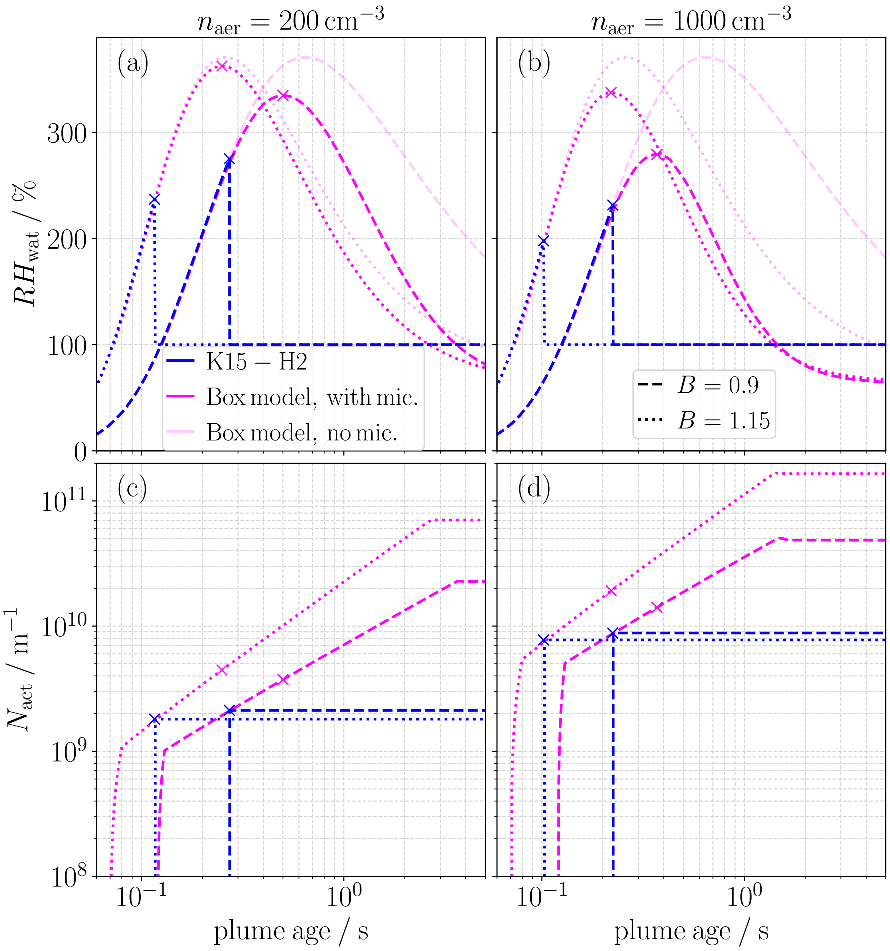

Figure 9. First row: Evolution of plume relative humidity over water RH_{wat} with peak values highlighted (crosses). Examples are shown for the ambient temperature $T_{\mathrm{a}} = 220\,\mathrm{K}$ and two aerosol number concentrations n_{aer} (columns). The evolutions according to the K15-H2 parameterization (blue) are compared to LCM box model simulation results (magenta). Dashed and dotted curves correspond to exponents $B = 0.9$ and $B = 1.15$ in Eq. (24), respectively. Results are presented for cases with microphysical water vapor depletion (opaque curves) and with microphysics switched off (transparent curves). Second row: Evolution of number of already activated aerosols N_{act} (sum of droplets and ice crystals in the box model) and the nucleation pulse for the K15-H2 parameterization with the values highlighted, where the relative humidity peaks (crosses).

https://doi.org/10.5194/egusphere-2026-1088
Preprint. Discussion started: 8 April 2026

most cases, $N_{\mathrm{act,peak,box}}$ remains significantly below the final number of ice crystals formed $N_{\mathrm{ice,box}}$ due to the continuous entrainment and activation of ambient aerosols long after $t = t_{\mathrm{peak,box}}$. The increase of $N_{\mathrm{act,peak}}$ with increasing T_{a} reflects the increase of t_{peak} with T_{a} (in both modeling approaches). In contrast, the decrease of $N_{\mathrm{ice,box}}$ with increasing T_{a} reflects the decreased duration of supersaturation and lower relative humidity peaks at higher ambient temperatures. Furthermore, the dilution-speed dependence is opposite between the two models. In line with Lewellen (2020) and Part 2 (Zink and Unterstrasser, 2025), slower dilution yields fewer ice crystals in the box model because early-activated aerosols have more time to consume the available water vapor and therefore suppress later activation more efficiently. The construction of the K15-H2 model, however, introduces a reversed dependency on dilution speed, even though the dependency is weak in our depicted examples.

The question that remains is why the droplets in the K15-H2 model are larger (Fig. 10e-f), which leads to much earlier supersaturation relaxation in K15-H2 (corresponding to $t_{\mathrm{peak,K15}} < t_{\mathrm{peak,box}}$). This can be explained as follows: At a given time t, the model looks backward to a past time t' when an aerosol particle would have been activated based on the aerosol dry spectrum at time t. As the K15 parameterization was originally developed for kerosene and ice crystal formation on emitted soot particles, it does not check, whether an aerosol particle present at time t was already present in the plume at t'. Thus, droplet growth is assumed to start at t', when the critical barrier is crossed according to κ-Köhler theory, even if the particle was entrained into the plume at a later time. This leads to an overestimation of growth time in K15-H2, producing larger droplets at earlier plume ages.

In summary, contrail formation on entrained ambient aerosols cannot be resolved by a parameterization assuming a nucleation pulse as it cannot realistically represent the water vapor depletion by continuously entrained and activated ambient aerosols. This continuous process is especially critical for hydrogen combustion, where supersaturation persists longer than for kerosene due to the higher water vapor emission index (Schumann, 1996; Bier et al., 2024). The K15 contrail ice formation parameterization was developed for aviation emissions within the soot-rich regime. Our analysis demonstrates that the K15 parameterization should not be applied in regimes where droplet formation on entrained particles is dominant.

4.2 Strengths and limitations of the parameterization

The parameterization relies on the outcome of time-resolved contrail formation simulations performed with the LCM box model, which includes detailed microphysics. The neural networks are employed as fitting functions of the simulation results, so that the parameterization does not introduce any assumptions beyond those in the original box model. Together with the provided scaling relations, the neural networks yield a generalized parameterization that captures the (nonlinear) influence of many variables on the ice crystal number. Although only a few calculations are needed (Eqs. (2a)–(2d)), the neural networks are flexible enough to capture the nonlinear dependence of the ice crystal number on the input variables. The underlying physics have been discussed in detail in Parts 1 and 2 (Zink et al., 2025a; Zink and Unterstrasser, 2025).

The neural networks are trained on a systematically constructed database without weighting data points (e.g., by the joint probability density function of climatology of ambient conditions, aerosol distributions, or air traffic). This approach ensures that the parameterization is broadly applicable. This includes a wide range of potential future scenarios, reflecting uncertainties

https://doi.org/10.5194/egusphere-2026-1088
Preprint. Discussion started: 8 April 2026

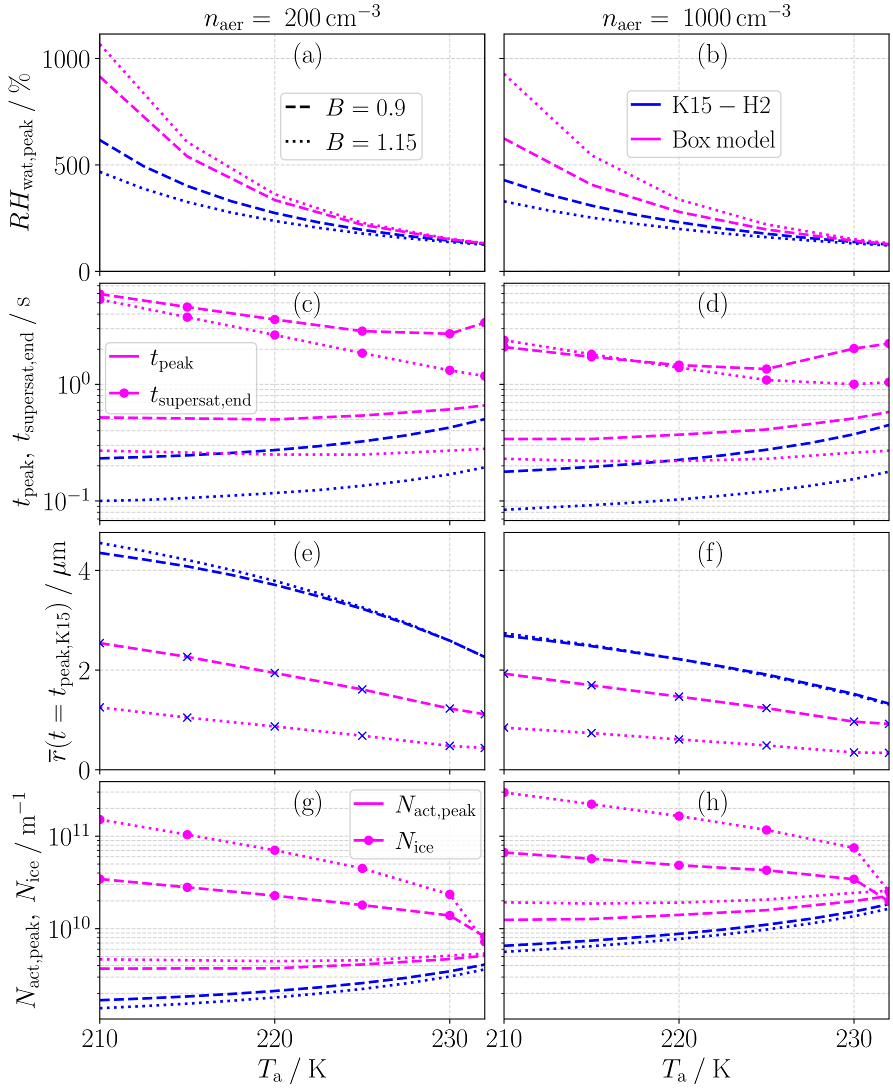

Figure 10. Comparison of the K15-H2 parameterization (blue) to LCM box model results (magenta). Dashed and dotted curves correspond to exponents $B = 0.9$ and $B = 1.15$ in Eq. (24). Results are shown as a function of ambient temperature T_{a} for two aerosol number concentrations n_{aer} (columns). Panels: (a)-(b) Peak value of plume relative humidity over water $RH_{\mathrm{wat,peak}}$. (c)-(d) Point in time t_{peak} at which plume relative humidity peaks. For the box model outcome, the point in time $t_{\mathrm{supersat,end}}$ is also depicted, where the relative humidity falls below 100 % (curves with magenta dots). (e)-(f) Mean radius of activated aerosols $\overline{r}(t = t_{\mathrm{peak,K15}})$ at the time of activation in the K15-H2. Box model results are evaluated at the same point in time $t = t_{\mathrm{peak,K15}}$ (magenta line with blue crosses). (g)-(h) Number of activated aerosols $N_{\mathrm{act,peak}}$ at the relative humidity peaks. The final number of ice crystals formed N_{ice} is shown for the box model results in addition (curves with magenta dots).

https://doi.org/10.5194/egusphere-2026-1088
Preprint. Discussion started: 8 April 2026

in climate projections, ambient aerosol loading, and air traffic evolution. Due to the gridded structure of the training database, the validity is well defined by the range spanned between the lower and upper grid values (Table 1).

As the neural networks consist of only a short sequence of calculations (Eqs. (2a)–(2d)), their implementation in large-scale models is straightforward. An alternative approach based on multidimensional lookup tables would require considerably more storage than the weight matrices and necessitate interpolation between tabulated points. Neural networks therefore offer a more compact and efficient way to integrate the box model simulation results into large-scale models. In addition, the proposed neural-network-based framework can be easily updated. Once a suitable training database is created, the neural networks can be retrained on a local machine within minutes. Updating the neural networks in large-scale models is equally simple, requiring only the replacement of the weights and biases.

The neural networks reproduce the box model results with the errors listed in Table 2 and any remaining limitation arises from the LCM box model itself. The LCM box model has been validated against other contrail formation models for conventional kerosene combustion with ice crystal formation on soot particles (Bier et al., 2022). Parameterizations of physical processes in the box model, particularly those relevant to hydrogen combustion, introduce additional uncertainty. For example, homogeneous freezing is modeled using a combined approach (Bier et al., 2024) that accounts for both the cooling rate (i.e., the change of supersaturation) (Riechers et al., 2013) and the solution effect of aqueous droplets (O and Wood, 2016). These parameterizations are based on laboratory measurements under conditions typical of natural cirrus clouds, which have lower turbulence and slower cooling rates than turbulent jets, making their applicability to contrail formation uncertain. Measurements at contrail formation conditions for which our simulations indicate a strong influence of homogeneous freezing (ambient temperatures $\gtrsim 230\,\mathrm{K}$) would be particularly valuable for validation.

A key uncertainty of the parameterization lies in the assumption that entrained ambient aerosols are the sole precursors of ice crystal formation. Recently, Zink et al. (2025b) demonstrated that even a very small amount of lubrication oil released into the exhaust (on the order of a few milliliters per hour or less) can produce large numbers of particles. When the oil enters the hot sections of the exhaust, it may evaporate and re-nucleate in the subsequent cooling plume, producing a nucleation-mode particle distribution (Ungeheuer et al., 2022). As such oil particles can activate into droplets and freeze into ice crystals (Ponsonby et al., 2024), a tiny amount of lubrication oil could already lead to oil-particle-dominated ice crystal formation (Zink et al., 2025b). The impact depends strongly on where the lubrication system vents. If venting occurs close to the hot core exit, entrainment into high-temperature regions promotes evaporation and re-nucleation. If the oil breather flow is released far away from the hot regions, the oil might be entrained into the plume when it has already cooled down such that it does not evaporate. These oil particles are then expected to be larger (a few hundred nanometers) and correspondingly fewer in number, thus contributing only little to ice crystal number. Thus, lubrication oil poses a potential concern for certain engine configurations, though technical measures to reduce or mitigate this effect may be feasible.

Furthermore, our simulations neglected the potential impact of NO_x emissions on contrail formation. In the exhaust plume, gaseous nitric acid (HNO_3) forms through oxidation of NO_x (Kärcher, 1995). This nitric acid may influence plume chemistry and contrail microphysics in two ways. First, HNO_3 could contribute to new particle formation, on which water vapor then condenses. While electrically neutral nitric acid alone may nucleate inefficiently, the presence of ions formed during the combustion process may enhance ion-induced nucleation (Yu and Turco, 1997; Kärcher et al., 2000). Clearly, the composition of ions and formation of volatile particles in the exhaust of aircraft burning hydrogen differs from that of conventional jet fuels, mainly because of the absence of sulfur and organic species in the fuel. Previous studies have additionally shown that nucleation is further facilitated in the presence of ammonia (Kirkby et al., 2023), which is not a direct emission product but is present in the ambient atmosphere. It remains an open question whether nitric acid–driven nucleation is efficient enough to contribute substantially to ice crystal formation and further research is needed to clarify its significance. Second, the uptake of highly soluble nitric acid by the entrained ambient aerosols could modify their chemical properties, which in principle could be represented by a time-dependent hygroscopicity. In our simulations, however, hygroscopicity values are prescribed at the beginning and remain constant throughout the simulation runs. Simulations for a wide range of prescribed hygroscopicity values (Table 1) showed that modest variations only marginally affect the number of ice crystals (Zink et al., 2025a). We therefore speculate that allowing hygroscopicity to vary slightly over time would likewise have little impact on the results, and the use of fixed hygroscopicity values is unlikely to introduce a substantial bias.

In summary, considering only entrained ambient aerosols as precursors, the presented ice crystal numbers represent an (idealized) lower limit. While other particle sources could, in principle, be reduced by technical measures, ambient aerosols cannot be removed and their abundance in the exhaust plume is constrained by their concentrations in the background atmosphere.

5 Conclusions

We developed a parameterization for the number of contrail ice crystals $N_{\mathrm{ice,f}}$ formed on entrained ambient aerosols for aircraft with hydrogen combustion. This parameterization can be integrated into large-scale models with a contrail parameterization to study the climate impact of contrails from an aviation fleet powered by hydrogen combustion. The parameterization combines a neural-network-based fit to a multidimensional database of time-resolved contrail formation simulations with analytical scaling relations. The comparison with a parameterization assuming a nucleation pulse and instantaneous supersaturation relaxation demonstrated that, for hydrogen combustion, a time-resolved database is essential in order to realistically capture the full contrail formation process on entrained ambient aerosols.

The provided functional relationship can be summarized as

$$\begin{aligned}
N_{\mathrm{ice,f}} &= N_{\mathrm{ice,f}}(\mathbf{a}_{\mathrm{atmosphere}}, \mathbf{a}_{\mathrm{aerosol}}, \mathbf{a}_{\mathrm{aircraft}}) \\
&= N_{\mathrm{ice,f}}(T_{\mathrm{a}}, p_{\mathrm{a}}, RH_{\mathrm{ice,a}}, \{n_{\mathrm{aer},i}, \overline{r}_{\mathrm{d,aer},i}, \kappa_{\mathrm{aer},i}\}_{i=1}^{N}, \eta, r_{\mathrm{E}}, U_{\mathrm{jet,E}}, U_{\infty}, n_{\mathrm{engines}}) \\
&\approx N_{\mathrm{ice,f}}(T_{\mathrm{a}}, p_{\mathrm{a}}, RH_{\mathrm{ice,a}}, \{n_{\mathrm{aer},i}, \overline{r}_{\mathrm{d,aer},i}, \kappa_{\mathrm{aer},i}\}_{i=1}^{N}, \eta, m_{\mathrm{C,tot}}, n_{\mathrm{engines}})\ .
\end{aligned} \tag{25}$$

It includes input variables describing the background atmosphere $\mathbf{a}_{\mathrm{atmosphere}}$, which are the ambient temperature T_{a}, ambient pressure p_{a} and ambient relative humidity $RH_{\mathrm{ice,a}}$. Moreover, it contains properties $\mathbf{a}_{\mathrm{aerosol}}$ of multiple aerosol populations i, namely the number concentration $n_{\mathrm{aer},i}$, geometric mean radius $\overline{r}_{\mathrm{d,aer},i}$ and hygroscopicity $\kappa_{\mathrm{aer},i}$. Finally, it incorporates aircraft-related parameters $\mathbf{a}_{\mathrm{aircraft}}$, which are the overall propulsion efficiency η, the engine core exit radius r_{E}, core exit excess jet speed $U_{\mathrm{jet,E}}$, aircraft speed U_{∞} and the number of engines n_{engines}. If information about engine size and jet speed is not available, than an approximation can be used that is based on the total fuel consumption of the aircraft $m_{\mathrm{C,tot}}$.

Appendix A: Parameterization cookbook

1. Calculate the adjusted pressure $p_{\mathrm{a,adj}}$ according to Eq. (17) to account for deviations of the actual overall propulsion efficiency η from the reference value η^* (Table 1).
2. Calculate the scaling factors s_{shear}, s_{E}, s_{dil} and $\hat{s}_{\mathrm{E}}$ according to Eqs. (18a)-(18d) accounting for differences in jet speed and engine size with associated change in dilution speed. If information is missing, then use the approximation after Eq. (22).
3. Determine the total aerosol number concentration $n_{\mathrm{aer,tot}} = \sum_i n_{\mathrm{aer},i}$ where the index i runs over all aerosol populations.
4. For each aerosol population, determine $N_{\mathrm{ice,param},i}$ by following the flow chart in Fig. A1. As inputs use ambient temperature T_{a}, adjusted ambient pressure $p_{\mathrm{a,adj}}$, ambient relative humidity $RH_{\mathrm{ice,a}}$, scaled total aerosol number concentration $s_{\mathrm{dil}}^{3/2} n_{\mathrm{aer,tot}}$, single aerosol population hygroscopicity $\kappa_{\mathrm{aer},i}$ and geometric mean dry radius $\overline{r}_{\mathrm{d,aer},i}$.
5. Multiply $N_{\mathrm{ice,param},i}$ by $\hat{s}_{\mathrm{E}}^2 s_{\mathrm{dil}}^a$ with a set according to Eq. (20).
6. Calculate the weighted mean after Eq. (16) to obtain the total ice crystal number $N_{\mathrm{ice,param,tot}}$.
7. Multiply $N_{\mathrm{ice,param,tot}}$ by the number of engines n_{engines} to obtain the ice crystal number for the whole aircraft, assuming that the individual plumes do not overlap during ice crystal formation.

Code and data availability. A python code following the steps described in Appendix A, along with the trained weight matrices, will be made available once the manuscript has been accepted. The LCM box model simulations used for training the neural networks are available in the Zenodo repository of Part 1 (https://doi.org/10.5281/zenodo.17977711).

Author contributions. JZ and SU conceptualized the study, with CWR and UB contributing in Sects 3.2 and 4.1. JZ performed the box model simulations and trained the neural networks. JZ created the tables and all figures except Fig. 8, which was produced by CWR. JZ wrote the first draft of the manuscript. All authors reviewed and edited the manuscript, particularly Sect. 4.1, which was developed collaboratively by all authors. SU and UB supervised the study.

Competing interests. The contact author has declared that none of the authors has any competing interests.

Acknowledgements. This work contributes to the DLR internal project “H2CONTRAIL”. All authors received funding from Airbus SAS. We thank Drago Jakimovski for performing part of the hyperparameter tuning during his DAAD internship. We acknowledge Ellen Sarauer

https://doi.org/10.5194/egusphere-2026-1088
Preprint. Discussion started: 8 April 2026

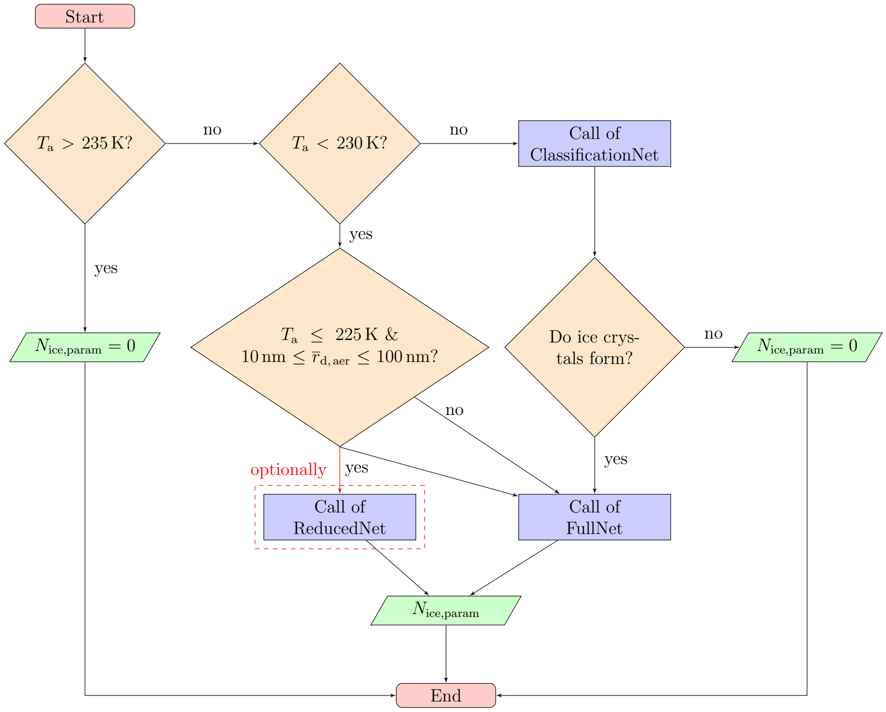

Figure A1. Flow chart for determining the parameterized ice crystal number for a single aerosol population and a single reference engine characterized by the parameter values defined in Table 1. For the subspace defined by $T_\mathrm{a} \leq 225\,\mathrm{K}$ and $10\,\mathrm{nm} \leq \overline{r}_\mathrm{d,aer} \leq 100\,\mathrm{nm}$, either the FullNet or the ReducedNet can be used.

for an internal review of the paper draft. Our thanks also go to Charles Renard for his valuable comments. The language was polished with the help of ChatGPT.

References

Bier, A. and Burkhardt, U.: Variability in Contrail Ice Nucleation and Its Dependence on Soot Number Emissions, J. Geophys. Res., 124, 3384–3400, https://doi.org/10.1029/2018JD029155, 2019.

Bier, A. and Burkhardt, U.: Impact of Parametrizing Microphysical Processes in the Jet and Vortex Phase on Contrail Cirrus Properties and Radiative Forcing, J. Geophys. Res., 127, e2022JD036 677, https://doi.org/10.1029/2022JD036677, 2022.

Bier, A., Burkhardt, U., and Bock, L.: Synoptic Control of Contrail Cirrus Life Cycles and Their Modification Due to Reduced Soot Number Emissions, J. Geophys. Res., pp. 11 584–11 603, https://doi.org/10.1002/2017JD027011, 2017JD027011, 2017.

Bier, A., Unterstrasser, S., and Vancassel, X.: Box model trajectory studies of contrail formation using a particle-based cloud microphysics scheme, Atmos. Chem. Phys., 22, 823–845, https://doi.org/10.5194/acp-22-823-2022, 2022.

Bier, A., Unterstrasser, S., Zink, J., Hillenbrand, D., Jurkat-Witschas, T., and Lottermoser, A.: Contrail formation on ambient aerosol particles for aircraft with hydrogen combustion: a box model trajectory study, Atmos. Chem. Phys., 24, 2319–2344, https://doi.org/10.5194/acp-24-2319-2024, 2024.

Bishop, C. M.: Pattern recognition and machine learning, Information Science and Statistics, Springer Science+Business Media, LLC, New York, NY, 2019.

Bock, L. and Burkhardt, U.: The temporal evolution of a long-lived contrail cirrus cluster: Simulations with a global climate model, J. Geophys. Res., 121, 3548–3565, https://doi.org/10.1002/2015JD024475, 2016.

Burkhardt, U. and Kärcher, B.: Process-based simulation of contrail cirrus in a global climate model, J. Geophys. Res., 114, D16 201, https://doi.org/10.1029/2008JD011491, 2009.

Burkhardt, U., Bock, L., and Bier, A.: Mitigating the contrail cirrus climate impact by reducing aircraft soot number emissions, npj Climate and Atmospheric Science, 1, 37, https://doi.org/10.1038/s41612-018-0046-4, 2018.

Etling, D.: Theoretische Meteorologie: Eine Einführung, https://doi.org/10.1007/978-3-540-75979-9, 2008.

Gettelman, A. and Chen, C.: The climate impact of aviation aerosols, Geophys. Res. Lett., 40, 2785–2789, https://doi.org/10.1002/grl.50520, 2013.

Kärcher, B.: A trajectory box model for aircraft exhaust plumes, J. Geophys. Res., 100, 18 835–18 844, 1995.

Kärcher, B.: Aviation-produced aerosols and contrails, Surveys in Geophysics, 20, 113–167, 1999.

Kärcher, B.: Formation and radiative forcing of contrail cirrus, Nature Communications, 9, 1824, https://doi.org/10.1038/s41467-018-04068-0, 2018.

Kärcher, B., Burkhardt, U., Bier, A., Bock, L., and Ford, I. J.: The microphysical pathway to contrail formation, J. Geophys. Res., 120, 7893–7927, https://doi.org/10.1002/2015JD023491, 2015.

Kirkby, J., Amorim, A., Baltensperger, U., Carslaw, K. S., Christoudias, T., Curtius, J., Donahue, N. M., Haddad, I. E., Flagan, R. C., Gordon, H., Hansel, A., Harder, H., Junninen, H., Kulmala, M., Kürten, A., Laaksonen, A., Lehtipalo, K., Lelieveld, J., Möhler, O., Riipinen, I., Stratmann, F., Tomé, A., Virtanen, A., Volkamer, R., Winkler, P. M., and Worsnop, D. R.: Atmospheric new particle formation from the CERN CLOUD experiment, Nature Geoscience, 16, 948–957, https://doi.org/10.1038/s41561-023-01305-0, 2023.

Kärcher, B., Turco, R. P., Yu, F., Danilin, M. Y., Weisenstein, D. K., Miake-Lye, R. C., and Busen, R.: A unified model for ultrafine aircraft particle emissions, J. Geophys. Res., 105, 29 379–29 386, https://doi.org/10.1029/2000JD900531, 2000.

Lee, D. S., Fahey, D. W., Skowron, A., Allen, M. R., Burkhardt, U., Chen, Q., Doherty, S. J., Freeman, S., Forster, P. M., Fuglestvedt, J., Gettelman, A., De León, R. R., Lim, L. L., Lund, M. T., Millar, R. J., Owen, B., Penner, J. E., Pitari, G., Prather, M. J., Sausen, R., and

Wilcox, L. J.: The contribution of global aviation to anthropogenic climate forcing for 2000 to 2018, Atmos. Environ., 244, 117 834, https://doi.org/10.1016/j.atmosenv.2020.117834, 2021.

Lewellen, D. C.: Persistent contrails and contrail cirrus. Part 2: Full Lifetime Behavior, J. Atmos. Sci., pp. 4420–4438, https://doi.org/10.1175/JAS-D-13-0317.1, 2014.

Lewellen, D. C.: A Large-Eddy Simulation Study of Contrail Ice Number Formation, J. Atmos. Sci., 77, 2585–2604, https://doi.org/10.1175/JAS-D-19-0322.1, 2020.

Lottermoser, A. and Unterstrasser, S.: High-resolution modeling of early contrail evolution from hydrogen-powered aircraft, Atmos. Chem. Phys., 25, 7903–7924, https://doi.org/10.5194/acp-25-7903-2025, 2025.

O, K.-T. and Wood, R.: Exploring an approximation for the homogeneous freezing temperature of water droplets, Atmos. Chem. Phys., 16, 7239–7249, https://doi.org/10.5194/acp-16-7239-2016, 2016.

Paoli, R. and Shariff, K.: Contrail Modeling and Simulation, Annu. Rev. Fluid Mech., 48, 393–427, https://doi.org/10.1146/annurev-fluid-010814-013619, 2016.

Petters, M. D. and Kreidenweis, S. M.: A single parameter representation of hygroscopic growth and cloud condensation nucleus activity, Atmos. Chem. Phys., 7, 1961–1971, https://doi.org/10.5194/acp-7-1961-2007, 2007.

Pettersson, S., Azar, C., and Johansson, D.: Climate impact of contrail cirrus from hydrogen combustion aircraft, EGUsphere, pp. 1–24, https://doi.org/10.5194/egusphere-2025-3535, 2025.

Ponsonby, J., King, L., Murray, B. J., and Stettler, M. E. J.: Jet aircraft lubrication oil droplets as contrail ice-forming particles, Atmos. Chem. Phys., 24, 2045–2058, https://doi.org/10.5194/acp-24-2045-2024, 2024.

Riechers, B., Wittbracht, F., Hütten, A., and Koop, T.: The homogeneous ice nucleation rate of water droplets produced in a microfluidic device and the role of temperature uncertainty, Physical Chemistry Chemical Physics, 15, 5873–5887, https://doi.org/10.1039/c3cp42437e, 2013.

Schumann, U.: On conditions for contrail formation from aircraft exhausts, Meteorol. Z., 5, 4–23, https://doi.org/10.1127/metz/5/1996/4, 1996.

Schumann, U.: A contrail cirrus prediction model, Geosci. Model Dev., 5, 543–580, https://doi.org/10.5194/gmd-5-543-2012, 2012.

Schumann, U., Penner, J. E., Chen, Y., Zhou, C., and Graf, K.: Dehydration effects from contrails in a coupled contrail-climate model, Atmos. Chem. Phys., 15, 11 179–11 199, https://doi.org/10.5194/acp-15-11179-2015, 2015.

Ungeheuer, F., Caudillo, L., Ditas, F., Simon, M., van Pinxteren, D., Kilic, D., Rose, D., Jacobi, S., Kürten, A., Curtius, J., and Vogel, A. L.: Nucleation of jet engine oil vapours is a large source of aviation-related ultrafine particles, Commun. Earth Environ., 3, 1–8, https://doi.org/10.1038/s43247-022-006, 2022.

Unterstrasser, S.: Properties of young contrails - a parametrisation based on large-eddy simulations, Atmos. Chem. Phys., 16, 2059–2082, https://doi.org/10.5194/acp-16-2059-2016, 2016.

Unterstrasser, S. and Gierens, K.: Numerical simulations of contrail-to-cirrus transition - Part 2: Impact of initial ice crystal number, radiation, stratification, secondary nucleation and layer depth, Atmos. Chem. Phys., 10, 2037–2051, https://doi.org/10.5194/acp-10-2037-2010, 2010.

Vancassel, X., Mirabel, P., and Garnier, F.: Numerical simulation of aerosols in an aircraft wake using a 3D LES solver and a detailed microphysical model, Int. J. Sustainable Aviation, 1, 139–159, https://doi.org/10.1504/IJSA.2014.065480, 2014.

Yu, F. and Turco, R. P.: The role of ions in the formation and evolution of particles in aircraft plumes, Geophys. Res. Lett., 24, 1927–1930, 1997.

Zink, J. and Unterstrasser, S.: Contrail formation for aircraft with hydrogen combustion - Part 2: Engine-related aspects, EGUsphere, pp. 1–34, https://doi.org/10.5194/egusphere-2025-3708, 2025.

625 Zink, J., Unterstrasser, S., and Burkhardt, U.: Contrail formation for aircraft with hydrogen combustion - Part 1: A systematic microphysical investigation, EGUsphere, pp. 1–27, https://doi.org/10.5194/egusphere-2025-3704, 2025a.

Zink, J., Unterstrasser, S., and Jurkat-Witschas, T.: On the Potential Role of Lubrication Oil Particles in Contrail Formation for Kerosene and Hydrogen Combustion, J. Geophys. Res., 130, https://doi.org/10.1029/2025jd043487, 2025b.